Research Square

Preprints are preliminary reports that have not undergone peer review.
They should not be considered conclusive, used to inform clinical practice,
or referenced by the media as validated information.

Ultrathin, High-Performance Circular Wave Plate Based on Natural van der Waals Crystals

Guowei Lu

guowei.lu@pku.edu.cn

Peking University https://orcid.org/0000-0003-0646-6971

Shuxin Huang

Peking University

Guanyu Zhang

Peking University https://orcid.org/0000-0001-9544-2300

Yaolong Li

Peking University https://orcid.org/0000-0002-1457-190X

Xianghan Meng

Peking University

Minghao Deng

Peking University

Yixuan Xu

Peking University

Zini Cao

Peking University

Jiaqi Li

Peking University

Qihuang Gong

Peking University https://orcid.org/0000-0003-4974-6244

Article

Keywords:

Posted Date: April 17th, 2026

DOI: https://doi.org/10.21203/rs.3.rs-9409027/v1

License: This work is licensed under a Creative Commons Attribution 4.0 International License.
Read Full License

Additional Declarations: There is **NO** Competing Interest.

Version of Record: A version of this preprint was published at Nature Communications on October 6th, 2026. See the published version at https://doi.org/10.1038/s41467-026-78564-z.

Ultrathin, High-Performance Circular Wave Plate Based on Natural van der Waals Crystals

Shuxin Huang, Guanyu Zhang, Yaolong Li, Xianghan Meng, Minghao Deng, Yixuan Xu, Zini Cao, Jiaqi Li, Qihuang Gong, and Guowei Lyu*

Abstract

Circularly polarized light (CPL) holds immense promise for diverse applications, including three-dimensional(3D) displays, quantum information processing, biosensing, and optical imaging. However, high-performance, ultrathin, and easily integrable devices for CPL manipulation and discrimination remain a significant challenge. Leveraging the phase modulation capability of the natural two-dimensional (2D) van der Waals material $NbOCl_2$ and the polarization selectivity of $MoOCl_2$, we propose and demonstrate a lithography-free, facilely fabricated, and ultrathin circular polarization wave plate. Experimental characterization demonstrates that the fabricated $MoOCl_2$/$NbOCl_2$ stacked nanoplates, with a thickness of merely ~690 nm, exhibit significant selectivity for left- and right-handed CPL across the visible spectrum, achieving a maximum extinction ratio of 14.72 dB. Furthermore, by integrating the stacked device into a light-emitting diode (LED) chip, we achieve high-quality circularly polarized emission is obtained at specifically designed wavelengths, with a degree of circular polarization (DOCP) reaching 98.72%. This work provides a versatile strategy for constructing ultrathin, integrable circularly polarized photonic devices by leveraging the intrinsic optical anisotropy of natural low-dimensional materials, and demonstrates broad application prospects in chiral light-field detectors and on-chip circularly polarized light sources.

Introduction

Circularly polarized light (CPL), as a pivotal information carrier in modern photonics, plays a crucial role in diverse fields such as 3D displays[1–3], quantum computing[4–6], remote sensing[7–9], and medical diagnostics[10–12]. Particularly, the efficient generation and precise discrimination of CPL states are fundamental prerequisites for chiral molecular detection and spin-based quantum information processing. To fully exploit the advantages of CPL in these scenarios, there is an urgent demand for integrated optoelectronic devices capable of high-performance CPL detection and manipulation[13].

Conventional CPL emission and filtering are typically based on linear polarizers paired with bulk birefringent crystals such as calcite, quartz, and MgF_2. However, these natural crystals have weak optical anisotropy in the visible band, with intrinsic birefringence generally below 0.3[14–19], requiring millimeter-scale thickness to accumulate sufficient phase retardation and thus inherently limiting device miniaturization. Meanwhile, during device thinning, polishing-induced surface roughness becomes increasingly prominent relative to the reduced thickness, which not only amplifies scattering losses, but also leads to phase distortion and efficiency degradation[20]. This

material-intrinsic size limitation hinders micro- and nano-integration and introduces significant wavefront errors, making conventional bulk circular polarizers unable to satisfy the urgent demands for miniaturization and high integration in modern ultra-compact on-chip integrated optical systems.

To address these limitations, researchers have explored artificially designed electromagnetic structures as a new strategy to enhance chiral interactions. Specifically,3D or quasi-3D helical metamaterials[21–23] can induce strong circular dichroism and high extinction ratios by introducing spatial helical symmetry. Nevertheless, these complex 3D structures typically require sophisticated fabrication processes and involve high production costs, which severely restricts their large-area scalability and practical industrial prospects. In the pursuit of further planarization and miniaturization, 2D optical metasurfaces have emerged as a promising candidate[24–26]. By introducing nanostructures at the sub-wavelength scale to induce interfacial phase discontinuities, metasurfaces can achieve precise control over polarization states within nanometer-scale thicknesses. Nonetheless, existing metasurface solutions remain constrained by the complexity of structural design and inadequate output DOCP. Consequently, exploring a natural material that simultaneously possesses giant intrinsic optical anisotropy and excellent process compatibility is crucial for realizing the next generation of ultra-thin polarization devices.

In this context, atomically thin 2D van der Waals (vdW) materials have risen to the forefront optics and optoelectronics over recent years. Their unique merits—atomically smooth surfaces that mitigate optical wavefront distortion, vdW interlayer bonding enabling low-defect heterointegration, and giant in-plane optical anisotropy compatible with high-density integrated devices—render them an unprecedented material platform for engineering strong optical anisotropy[27].

However, the majority of reported layered van der Waals (vdW) materials to date host optical axes aligned along the out-of-plane direction, rendering them incompatible with practical implementation in ultra-thin polarization photonic devices[28–30]. While biaxial 2D vdW materials typified by black phosphorus (BP) and rhenium disulfide (ReS_2) possess intrinsic in-plane optical anisotropy[31,32], their optical dichroism and birefringence amplitude in the visible(VIS) to near-infrared(NIR) band remain fundamentally limited, severely restricting their use in high-performance polarization devices[33]. Recent advances in the emerging 2D vdW materials $NbOCl_2$[34–37] and $MoOCl_2$[38–43] with strong in-plane anisotropy, have opened up new avenues to address the aforementioned challenges. $NbOCl_2$ demonstrates extraordinary in-plane birefringence across a broad spectral range from the VIS to NIR, serving as an ideal material system for high-efficiency waveplate devices[33]. Likewise, $MoOCl_2$ exhibits metallic reflection behavior along the x-direction ([100]) and dielectric transmission behavior along the y-direction([010])[44](Fig.1d), making it an outstanding material for high-performance linear polarizers[40]. Consequently, $MoOCl_2$ and $NbOCl_2$ with giant intrinsic anisotropy provide an ideal platform for developing circular polarization devices; however, waveplate devices based on these materials remain scarce.

In this work, we leverage the giant intrinsic anisotropy of natural vdW materials $MoOCl_2$ and $NbOCl_2$ to successfully construct a high-performance, ultrathin circular polarization wave plate. The working principle is schematically illustrated in Fig.1a. By utilizing the phase modulation capability of $NbOCl_2$ and the polarization selectivity of $MoOCl_2$, we achieve efficient discrimination of circularly polarized light without the need for complex nanofabrication. Experimental results demonstrate that the fabricated circular polarization wave plate achieves a maximum extinction ratio of 14.72 dB in the visible range. Furthermore, the wave plate can be integrated with LED chips to achieve high-quality circularly polarized light emission at specific wavelengths, reaching a DOCP of 98.72%. This work provides a more concise and feasible pathway for implementing photonic functional devices by exploiting the intrinsic physical properties of low-dimensional materials, and offers a practical solution for the construction of integrated low-dimensional optical systems.

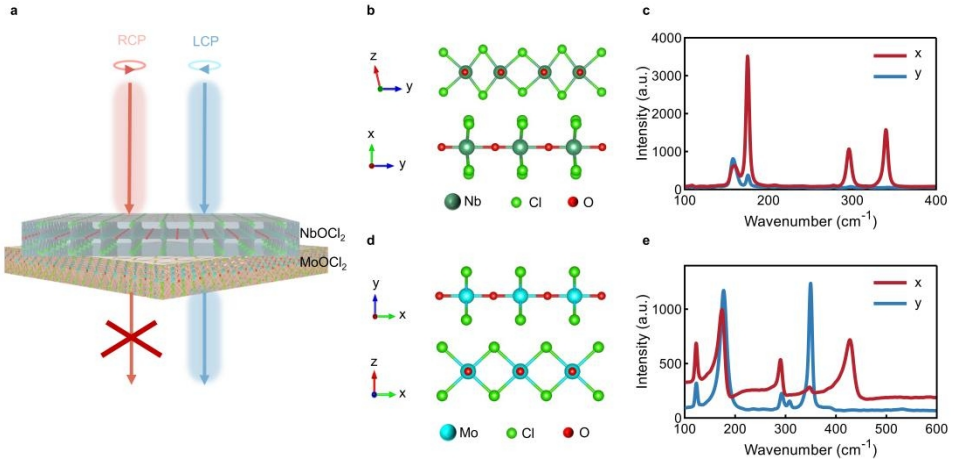


Fig.1. Principle of the natural ultrathin, high-performance circular polarization wave plate. (a) Schematic diagram of the working principle of the ultrathin high-performance circular polarization wave plate based on natural materials. (b) Schematic illustration of the crystal structure of $NbOCl_2$. (c) Raman spectra of $NbOCl_2$ excited by orthogonal polarization. (d) Schematic illustration of the crystal structure of $MoOCl_2$. (e) Raman spectra of $MoOCl_2$ excited by orthogonal polarization.

Results

1. Theoretical Analysis and Design of the Chiral-Discriminating Stacked Structure

The crystal structure of $NbOCl_2$ is composed of distorted $NbCl_4O_2$ octahedral units (Fig.1b), which form a unique layered structure via corner- and edge-sharing[33]. Fig.1c provides the Raman spectra of $NbOCl_2$ along the x and y directions, which, combined with Fig.S2, further validate its remarkable in-plane anisotropy. The crystal structure of natural $MoOCl_2$ belongs to the monoclinic system (Fig.1d), where Mo-O chains extend along the [100] direction and are sandwiched by chlorine atom layers, resulting in robust in-plane anisotropy[39,45]. This structural configuration gives rise to distinct optical

responses along two orthogonal in-plane directions, making $MoOCl_2$ an exceptional material for high-performance linear polarizers. Fig.1e displays the Raman spectra of $MoOCl_2$ along the x and y directions, and Fig.1e together with Fig.S1 further confirm its pronounced in-plane anisotropy.

To systematically investigate the linear polarization-selective transmission characteristics of $MoOCl_2$, we performed finite-difference time-domain (FDTD) simulations to calculate its transmittance across a thickness range of 100 nm to 600 nm. The complex dielectric function of $MoOCl_2$ used in the simulations was experimentally determined via spectroscopic ellipsometry. The simulation setup is illustrated in Fig.2a, where the response of $MoOCl_2$ to different linear polarizations was analyzed by varying the polarization angle of the incident light. Fig.2b and c depict the evolution of transmittance as a function of $MoOCl_2$ thickness and incident wavelength for x-polarized (T_x) and y-polarized (T_y) light, respectively. Notably, T_y is consistently higher to T_x, representing a significant polarization-dependent transmittance difference. This behavior originates from the fact that the extinction coefficient of $MoOCl_2$ along the x-axis is substantially larger than that along the y-axis (Fig.S2a). As shown in Fig. 2b, T_x remains near zero across the majority of the wavelength and film thickness(d_1), with a single faint transmission peak observed exclusively at ~500 nm wavelength and ~100 nm thickness. Tx decays rapidly as the wavelength redshifts into the long-wavelength visible band and NIR regime, or as the film thickness increases beyond 300 nm. This strong extinction stems from the intense absorption and reflection of light polarized along the Mo-O atomic chains. As shown in Fig.2c, the Ty distribution exhibits obvious periodic oscillation characteristics. As the $MoOCl_2$ thickness increases, the transmission maxima shift across different wavelengths, forming a "slant-fringe" pattern. This oscillatory behavior is attributed to the Fabry–Pérot (F-P) cavity effect formed between the upper and lower surfaces of the material, where $MoOCl_2$ acts as a low-loss dielectric slab along the y-direction[40]. To quantitatively evaluate the linear polarization selectivity of $MoOCl_2$, Fig.2d presents the ratio of y-polarized to x-polarized transmittance as a function of thickness and wavelength. The results demonstrate that this ratio exceeds 1000 over a broad spectral range from 533 nm to 1000 nm. This confirms that $MoOCl_2$ possesses giant intrinsic linear dichroism, making it an exceptional candidate for high-performance linear polarizers and providing a foundation for its application in polarization control and chiral optics.

For an ideal quarter-wave plate (QWP), the relationship between thickness, operating wavelength, and material birefringence is governed by:

$$d_2 = m\frac{\lambda}{4\Delta n}$$

where d_2 is the thickness of $NbOCl_2$, m is the integer that indicates the order of the wave plate, λ is the incident wavelength, and Δn represents the in-plane birefringence. According to this relation, the QWP condition can be satisfied at specific wavelengths by precisely tailoring the thickness of the $NbOCl_2$ flake. The significant in-plane anisotropy of $NbOCl_2$ provides the physical basis for realizing ultrathin, natural birefringence-based

QWPs.

To systematically evaluate the QWP performance of $NbOCl_2$ in the visible regime, FDTD simulations were conducted to analyze its optical response from 400 nm to 1000 nm. The dielectric function of $NbOCl_2$ was adopted from the theoretical calculations by Mortazavi et al. [38]. The simulation model is shown in Fig.2e, using a circularly polarized incident source. Fig.2f shows the transmittance of $NbOCl_2$ under left-handed circularly polarized (LCP) illumination as a function of thickness and wavelength, with the white dashed lines indicating the positions where the phase retardation reaches 0 and π. These results suggest that by selecting an appropriate $NbOCl_2$ thickness, the required phase delay can be achieved at the target wavelength with high transmittance, allowing $NbOCl_2$ to function effectively as a QWP.

To further investigate the polarization evolution under CPL incidence, the output polarization distributions for LCP and RCP incidence are illustrated in Fig. 2g and 2h, respectively. The results demonstrate that CPL can be transformed into linearly polarized light (LPL) at the target wavelength upon passing through a specific thickness of $NbOCl_2$. Further analysis reveals that the polarization direction of the resulting LPL exhibits a distinct offset angle relative to the x-axis of the $NbOCl_2$ crystal. Consequently, to achieve optimal chiroptical discrimination within the $MoOCl_2/NbOCl_2$ stacked structure, it is necessary to twist the crystal orientation of the $MoOCl_2$ layer relative to that of the $NbOCl_2$ layer (Supplementary Section 2). A comparison between Fig. 2g and 2h indicates that the polarization direction of the output LPL under RCP incidence maintains a symmetric relationship with that under LCP incidence. This characteristic serves as the fundamental mechanism for the effective discrimination between LCP and RCP states.

Based on the simulation results above, we establish a theoretical model for the two-layer stacked structure device: the $NbOCl_2$ thin film utilizes its in-plane birefringence effect as an ultrathin quarter-wave plate to achieve phase delay modulation, while the $MoOCl_2$ thin film, with its strong linear dichroism, serves as a high-performance polarization-selective layer. By integrating phase modulation and polarization filtering via the stacked architecture, we achieve chiral discrimination of circularly polarized light. To further explore the influence of the thickness combination of $MoOCl_2$ and $NbOCl_2$ on chiral discrimination performance, we systematically simulated the transmission spectra for various thickness combinations using LCP and RCP incident light sources, and the simulation results of the corresponding transmittance ratios are shown in Fig.2j-l. The results indicate that the maximum transmittance ratio generally increases with the total thickness of the stack. Furthermore, different thickness combinations enable significant chiral discrimination across different spectral bands, where the thickness of $NbOCl_2$ mainly tunes the operating wavelength and the thickness of $MoOCl_2$ mainly determines the extinction ratio. These results demonstrate that by optimizing the geometric parameters of the $MoOCl_2/NbOCl_2$ stacked structure, high-extinction-ratio circular polarization discrimination can be achieved over a wide spectral range.

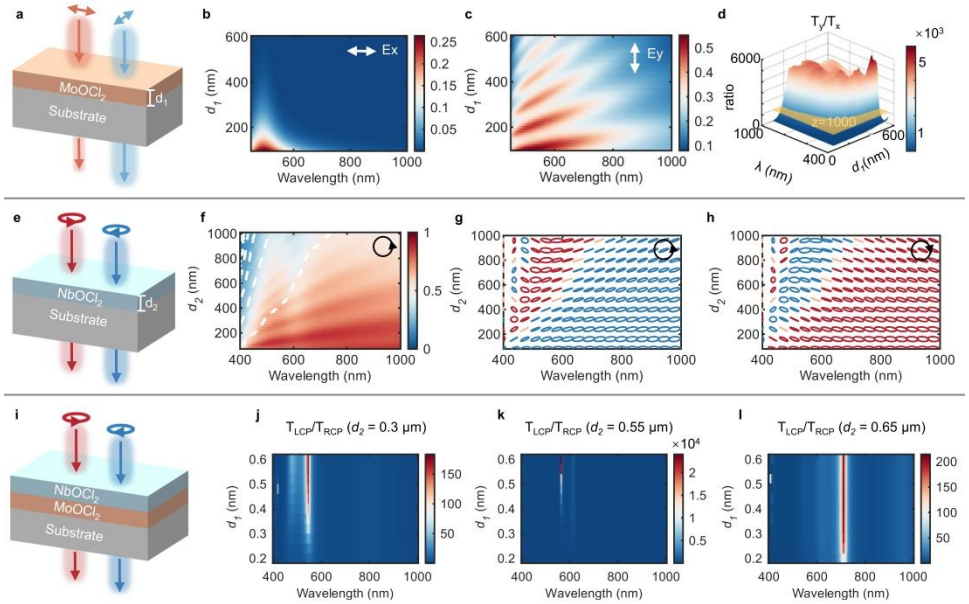


Fig.2. Theoretical analysis of the chiral-discriminating stacked structure. (a) Simulation model of $MoOCl_2$. (b-c) Transmission as a function of $MoOCl_2$ thickness (d_1) and incident wavelength for x-polarized (b) and y-polarized (c) incident light. (d) Ratio of the transmission for y-polarized light to that for x-polarized light as a function of d_1 and wavelength. (e) Simulation model of $NbOCl_2$. (f) Transmission of the outgoing light for LCP incidence as a function of $NbOCl_2$ thickness (d_2) and wavelength, where the white dashed lines indicate the positions corresponding to phase shifts of 0 and π. (g-h) Polarization state distribution of the transmitted light through the $NbOCl_2$ layer under LCP (g) and RCP (h) incidence, where red, blue, and orange represent right-handed polarization, left-handed polarization, and linear polarization, respectively. (i) Simulation model of $MoOCl_2/NbOCl_2$ stacked structures. (j-l) Transmission ratios of LCP to RCP after passing through $MoOCl_2/NbOCl_2$ stacked structures with different thickness combinations.

2. Experimental Realization of the Chiral-Discriminating Stacked Structure

Guided by the aforementioned simulations, we employed the mechanical exfoliation method to obtain $MoOCl_2$ and $NbOCl_2$ flakes with thicknesses of approximately 380 nm and 310 nm, respectively. Subsequently, a $MoOCl_2/NbOCl_2$ stacked structure was fabricated using a dry-transfer technique with a twist angle of approximately 45°.

2.1 $MoOCl_2$ as a linear polarizer

To investigate the intrinsic optical properties of 2D $MoOCl_2$, we characterized the transmittance spectra of the approximately 380 nm thick $MoOCl_2$ using a classical transmission optical path. To eliminate spectral contributions from materials surrounding the target flake, the field aperture was reduced to its minimum during measurement. The spectrum obtained from a bare glass coverslip was used as the blank for normalization of the sample transmission data.

The measurement schematic is shown in Fig.3a, where a linear polarizer (LP) was used to generate x- and y-polarized incident light. The thickness of the $MoOCl_2$ flake used

in our experiments was characterized by atomic force microscopy (AFM), with the result presented in Fig. 3b, which yields a measured thickness of 380 nm. Fig.3c presents the measured transmission spectra under x- and y-polarized incidence (red and blue curves, respectively), with the insets show optical micrographs of the flake under the two polarization conditions. When the incident polarization is aligned along the x direction, the $MoOCl_2$ region is almost non-transmitting and the overall transmission is very low. In contrast, under y-polarized incidence the flake is markedly more transmissive. Across the visible band T_y is consistently and significantly higher than T_x, directly demonstrating strong in-plane optical anisotropy of $MoOCl_2$. More specifically, T_x is low and exhibits a single peak, indicating strong absorption and reflection for x-polarization. T_y shows two pronounced transmission peaks in the 500-700 nm window, which we attribute to multiple-reflection interference within a F-P cavity formed by the flake surface, leading to enhanced transmission at specific wavelengths. To quantify the polarization selectivity, the ratio of Ty to Tx is presented in Fig. 3d. The results show that a 380 nm-thick $MoOCl_2$ film achieves a high extinction ratio approaching 20 dB in the 600-700 nm wavelength range, indicating its remarkable application potential as an ultrathin linear polarizer in the visible spectral region.

2.2 $NbOCl_2$ as a QWP

To verify the in-plane optical anisotropy and the response to CPL of 2D $NbOCl_2$, we measured the transmission spectra of LCP passing through the approximately 310 nm thick $NbOCl_2$ flake and calculated the ratio of transmittance along the x and y directions of the $NbOCl_2$.

The experimental configuration is depicted in Fig.3e. LCP light was generated using a circular polarizer, and an LP in the collection path was used to measure the output transmittance in the orthogonal x and y directions. The thickness of the $NbOCl_2$ flake was characterized by AFM, with the result presented in Fig. 3f, which yields a measured thickness of 310 nm. Fig.3g shows the transmission spectra along the x (red line) and y (blue line) directions after LCP incidence, with insets showing optical micrographs under x and y orientations. A clear contrast is observed: the sample exhibits low transmittance along the x-direction, whereas it is highly transparent along the y-direction. This substantial difference in orthogonal transmittance reflects the significant phase retardation induced by the material. Furthermore, Fig.3h presents the ratio of the y-component to the x-component of the transmitted light under LCP excitation. For the 310 nm thick $NbOCl_2$ sample, the degree of linear polarization (DOLP) of the modulated CPL reaches a maximum of 97.9%. This confirms that the material effectively transforms circularly polarized light into high-purity linearly polarized light, demonstrating excellent QWP characteristics. Thus, it serves as an ideal candidate for polarization state manipulation in micro-nano optical systems.

2.3 $MoOCl_2$/$NbOCl_2$ stack as a circular-polarization wave plate

To validate the chiral light-field discrimination performance of the stacked structure,

we measured its transmission spectra under LCP and RCP incidence across a wavelength range of 400-700 nm.

Fig.3i shows the experimental schematic, where LCP and RCP were produced using respective circular polarizers. Fig.3j displays the transmission spectra of the stacked structure under LCP (red line) and RCP (blue line) incidence, with the insets showing the corresponding optical micrographs. The stacked region displays high optical contrast between polarizations: it is high transmission under LCP incidence but remains opaque under RCP light, with the latter showing consistently low transmittance across the visible range. These observations confirm the intrinsic chiral selectivity of the fabricated stacked structure, which effectively suppresses the transmission of one handedness while maintaining high transparency for the other. Quantitatively, Fig.3k presents the T_{LCP}/T_{RCP} ratio across the visible spectrum. As shown in Fig.3j and 3k, at a wavelength of 581.6 nm, T_{LCP} reaches 0.452 while T_{RCP} is only 0.0152, yielding a high extinction ratio T_{LCP}/T_{RCP} of 29.677 (14.72 dB). This performance highlights the stacked structure's efficacy as an ultrathin chiral wave plate. Notably, the $MoOCl_2/NbOCl_2$ stacked structure exhibits remarkable stability: after six months of ambient storage, it retains robust chiral resolution, with the T_{LCP}/T_{RCP} ratio decreasing by only 14% (Fig.S6).

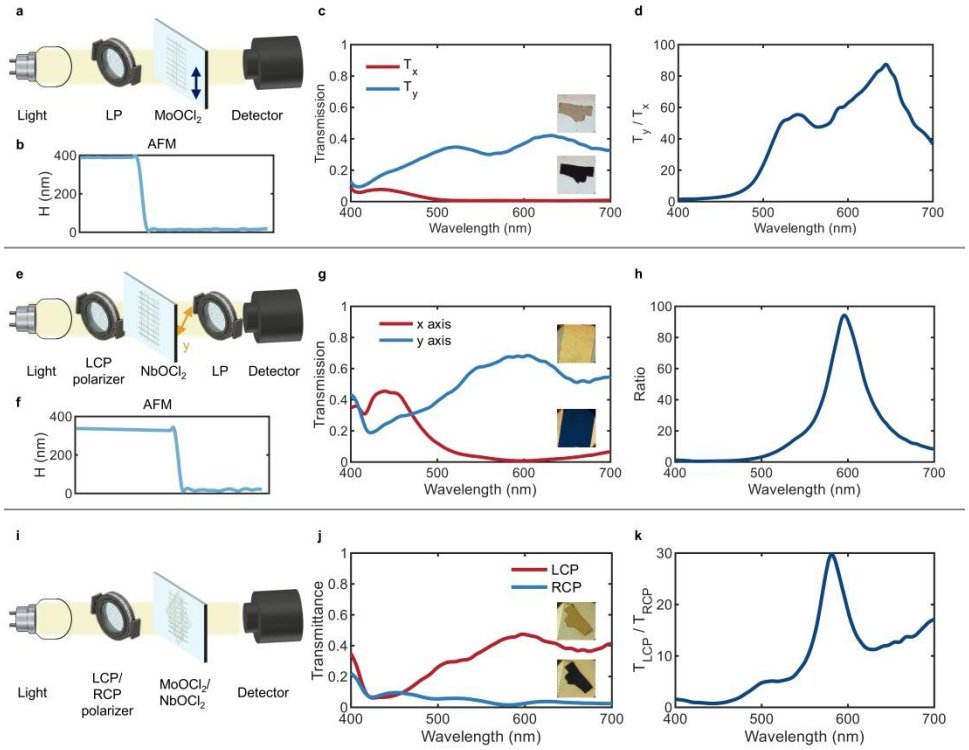


Fig.3. Experimental results of the chiral-discriminating stacked structure. (a) Optical setup for $MoOCl_2$ transmission measurements. (b) AFM characterization of the $MoOCl_2$ flake. (c) Transmission spectra of a 380 nm thick $MoOCl_2$ flake under x- and y-polarized illumination; the red and blue curves correspond to the measured T_x and T_y, respectively. Insets: transmission optical micrographs under the two polarization states. (d) Ratio T_y/T_x for the 380 nm $MoOCl_2$ flake. (e) Optical setup for $NbOCl_2$ transmission measurements. (f) AFM

characterization of the $NbOCl_2$ flake. (g) Transmission spectra of a 310 nm thick $NbOCl_2$ sample under LCP incidence, measured along the x (red line) and y direction (blue line). Insets: optical micrographs captured under LCP illumination with the analyzer aligned along the x and y directions at the output. (h) Ratio of the transmission measured with the analyzer aligned along the y direction to that along the x direction for the 310 nm $NbOCl_2$ sample. (i) Optical setup for measuring the transmission spectra of the $MoOCl_2/NbOCl_2$ stacked structure. (j) Transmission spectra of the stacked structure under LCP (red) and RCP (blue) incidence. Insets: corresponding optical micrographs. (k) Transmission ratio T_{LCP}/T_{RCP} of the $MoOCl_2/NbOCl_2$ stacked structure in the visible spectral range.

3. CPL-Emission-Chip Based on $MoOCl_2/NbOCl_2$ Stacked Structures

CPL sources underpin a diverse range of frontier applications including spanning chiral information control, spin-optoelectronic devices, and polarization-multiplexed optical communications. Integrating the fabricated 2D stacked structure in reverse as on-chip polarization elements with LED chips enables integrated manipulation of the emitted polarization state of unpolarized LEDs, producing on-chip circularly polarized emission without the need for bulky external polarization optics.

Fig.4a illustrates the schematic of the optical setup designed for characterizing the integrated circularly polarized light-emitting chip. The $MoOCl_2/NbOCl_2$ vdW stacked structure samples were integrated onto the light-emitting regions of LEDs with center wavelengths(λ_0) of 580nm and 450nm, respectively. To evaluate the chiroptical modulation imposed by the stacked structure, we performed polarization-resolved measurements by rotating a linear polarizer in the collection path to record the output intensity distribution at varying angles. As shown in Fig.4b, for the 580nm LED, the intensity of the transmitted electric field is nearly equal at all polarization detection, exhibiting negligible directional dependence. This confirms that the $MoOCl_2$/ $NbOCl_2$ stacked structure can effectively transform the initially unpolarized LED emission into near-ideal CPL, achieving a DOCP as high as 98.72%. Conversely, the 450 nm LED integrated with the same stacked structure exhibits a pronounced anisotropic intensity distribution (Fig.4c). This suggests a mismatch between the specific thickness combination of the $MoOCl_2$/ $NbOCl_2$ stack and the 450nm wavelength, underscoring the wavelength selectivity inherent in its chiral modulation capability.

Based on the theoretical analysis in “1. Theoretical Analysis and Design of the Chiral-Discriminating Stacked structure”, the extinction ratio can be optimized for any target wavelength by precisely tailoring the thicknesses of $MoOCl_2$ and $NbOCl_2$, where the thickness of $NbOCl_2$ mainly tunes the operating wavelength and the thickness of $MoOCl_2$ mainly determines the extinction ratio. Consequently, the $MoOCl_2$/ $NbOCl_2$ vdW stacked structure demonstrates significant potential not only in the realm of polarimetric detection but also for chiral-induced emission in light sources like lasers and LEDs, offering a novel material and structural paradigm for on-chip integrated circularly

polarized sources.

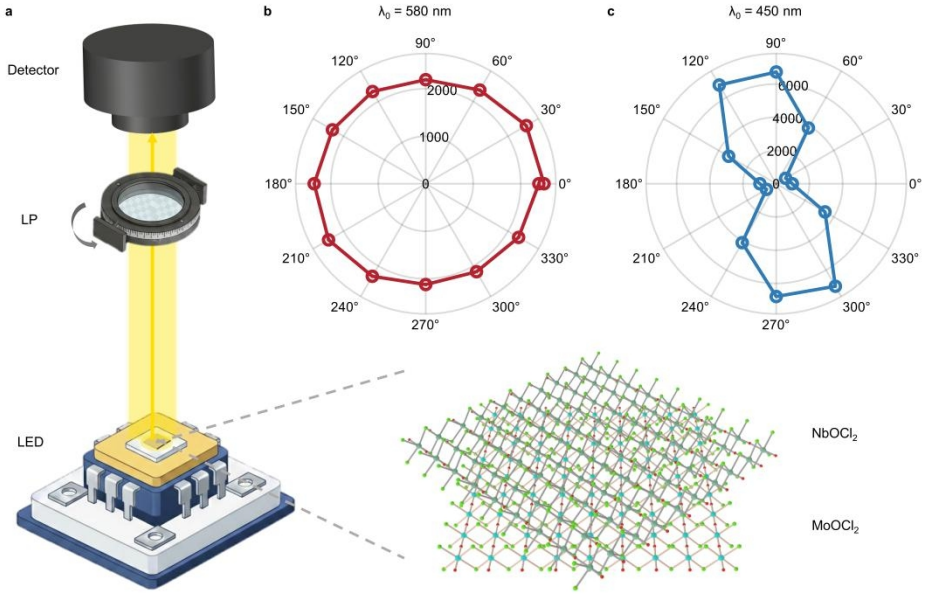


Fig.4. Integrated CP-LED chip based on $MoOCl_2$/$NbOCl_2$ stacked structures. (a) Schematic of the experimental configuration for characterizing the integrated circularly polarized light-emitting chip. (b, c) Polarization-resolved output intensity distributions of the CP-LEDs with central wavelengths of 580 nm (b) and 450 nm (c). The intensities were recorded by rotating a polarizer after the LED emission passed through the $MoOCl_2$/$NbOCl_2$ stacked structure.

Conclusion

In summary, we have systematically investigated and demonstrated an ultrathin, high-performance CPL wave plate based on the natural vdW materials $MoOCl_2$ and $NbOCl_2$. Theoretical analysis and FDTD simulations reveal that $MoOCl_2$ exhibits robust linear dichroism in the visible regime, serving as a high-performance linear polarizer, while $NbOCl_2$ functions as a sub-micron QWP due to its significant in-plane birefringence. By judiciously designing the thicknesses and twist angles of the two constituent materials, we constructed $MoOCl_2$/ $NbOCl_2$ stacked structures with exceptional chiral resolution. Experimental results confirm a distinct transmission response for LCP and RCP light, yielding a high extinction ratio of 14.72 dB at approximately 581.6 nm. Furthermore, we demonstrated an integrated CP-LED chip with a DOCP reaching 98.72%.

While this work focuses on the visible spectrum, considering that $NbOCl_2$ maintains excellent in-plane birefringence and $MoOCl_2$ exhibits stable strong linear dichroism with a broad low-loss operating window[40], both covering the VIS to NIR band, the proposed platform can be conveniently extended to other target spectral regions. This work demonstrates multiple outstanding advantages including high extinction ratio,

ultra-compact integration, low phase aberration, and excellent spectral scalability, with broad application prospects in frontier fields such as microfluidic biosensing, quantum computing, polarization-multiplexed optical communications, and chiral photodetection, and provides a practical and feasible solution for the design of low-dimensional heterointegrated optical devices and next-generation on-chip chiral photonic systems.

Methods

Preparation and Characterization of 2D Thin Flakes

Mechanical exfoliation was employed as the standard technique for the preparation of 2D monolayers. High-quality bulk crystals of $NbOCl_2$ and $MoOCl_2$ were purchased from Nanjing Moke Nano Technology Co., Ltd. Low-adhesivity polydimethylsiloxane (PDMS, 500 μm thickness, Sylgard 184) served as the transfer substrate. Small bulk crystal flakes were initially adhered to high-tack polyimide tape and then subjected to repeated exfoliation (2-3 cycles) to achieve reduced thickness. The resulting thin flakes were brought into contact with the PDMS substrate and slowly peeled away.

Preliminary screening for flakes with optimal thickness and superior surface morphology was conducted using an optical microscope (Olympus BX53). To ensure thickness uniformity and structural integrity, the selected candidates were further characterized via AFM and Raman spectroscopy. AFM topography was acquired using a HORIBA SmartSPM, while Raman spectra were collected with a HORIBA Scientific LabRAM HR Evolution system.

Construction of Stacked Wave Plates via Dry-Transfer Technique

In this work, the dry-transfer method was utilized to integrate mechanically exfoliated $MoOCl_2$ onto ITO substrates and to construct $NbOCl_2/MoOCl_2$ stacked structures. The specific procedure is as follows: A heating stage was used to maintain the temperature at ~80°C, thereby reducing the adhesion between the 2D material and the PDMS carrier. The glass slide supporting the target flake was fixed and precisely aligned using a high-precision 3D translation stage (Thorlabs MAX313D). The PDMS/2D material composite was lowered onto the target substrate at a controlled descent speed of 0.1 μm/s. Once full contact was established, the glass slide was retracted at the same velocity to complete the transfer.The transmitted light intensity images were recorded using a monochrome CMOS camera, the Tucsen Dhyana 400BSI V3.

Transmission Spectra and Light Intensity Measurements

Optical transmission spectra were measured using a custom-built microspectroscopy system integrated with an Olympus BX51WI microscope and an Ocean Insight QE Pro spectrometer, coupled via an optical fiber. A halogen lamp served as the broadband light source. To generate x- and y-linear polarization, as well as LCP and RCP, a rotatable linear polarizer and a quarter-wave plate or circular polarizer were inserted into the optical path. All transmission data were normalized against a clean, transparent glass slide to serve as the baseline reference.

Data availability

The data supporting the findings are displayed in the main text and the Supplementary Information. All raw data are available from the corresponding authors upon request.

Code availability

Codes supporting the results of this work are available from the corresponding authors upon request.

Acknowledgements

This work was supported by the National Key Research and Development Program of China (Grant No. 2024YFA1209201 and 2022YFA1604304) and the National Natural Science Foundation of China (Grant No. 12574405 and 92250305). We also thank the State Key Laboratory of Regional Fiber Optic Communication Networks and Novel Optical Communication Systems for nanofabrication facility support.

Reference

1. Gao, X. *et al.* Circularly polarized light emission from a GaN micro-LED integrated with functional metasurfaces for 3D display. *Opt. Lett.* **46**, 2666 (2021).
2. Guo, Q. *et al.* Self-positioning microdevices enable adaptable spatial displaying. *Science AdvAnceS* (2025).
3. Zhang, M. *et al.* Processable circularly polarized luminescence material enables flexible stereoscopic 3D imaging. *Sci. Adv.* **9**, eadi9944 (2023).
4. Wagenknecht, C. *et al.* Experimental demonstration of a heralded entanglement source. *Nature Photon* **4**, 549–552 (2010).
5. Sherson, J. F. *et al.* Quantum teleportation between light and matter. *Nature* **443**, 557–560 (2006).
6. Togan, E. *et al.* Quantum entanglement between an optical photon and a solid-state spin qubit. *Nature* **466**, 730–734 (2010).
7. Talmage, D. A. & Curran, P. J. Remote sensing using partially polarized light. *International Journal of Remote Sensing* **7**, 47–64 (1986).
8. Nagdimunov, L., Kolokolova, L. & Mackowski, D. Characterization and remote sensing of biological particles using circular polarization. *Journal of Quantitative Spectroscopy and Radiative Transfer* **131**, 59–65 (2013).
9. Luo, J. *et al.* Polarization properties of receiving telescopes in atmospheric remote sensing polarization lidars. *Appl. Opt.* **56**, 6837 (2017).
10. Van Eeckhout, A. Polarimetric methods for the image enhancement in biological applications. *Opt. Pura y Apl.* **57**, (2024).
11. Kunnen, B. *et al.* Application of circularly polarized light for non-invasive diagnosis of cancerous tissues and turbid tissue-like scattering media. *Journal of Biophotonics* **8**, 317–323 (2015).
12. Lu, D. *et al.* Cellulose Nanocrystal Films with NIR-II Circularly Polarized Light for Cancer Detection Applications. *ACS Nano* **17**, 461–471 (2023).
13. Hu, X. & Feng, Y. A Review on Recent Progress in Circularly Polarized Light Photodetector. *Research & Reviews: Journal of Material Sciences* **11**, 1–22 (2024).
14. Ghosh, G. Dispersion-equation coefficients for the refractive index and birefringence of calcite and quartz crystals. *Optics Communications* **163**, 95–102 (1999).
15. Sinton, W. M. Birefringence of Rutile in the Infrared. *J. Opt. Soc. Am.* **51**, 1309_1 (1961).
16. Luo, H. T., Tkaczyk, T., Dereniak, E. L., Oka, K. & Sampson, R. High birefringence of the yttrium vanadate crystal in the middle wavelength infrared. *Opt. Lett.* **31**, 616 (2006).
17. Guoqing, Z. *et al.* Growth and spectrum of a novel birefringent a-BaB_2O_4 crystal. *Journal of Crystal Growth* **191**, 517—519 (1998).
18. Tudi, A., Han, S., Yang, Z. & Pan, S. Potential optical functional crystals with large birefringence: Recent advances and future prospects. *Coordination Chemistry Reviews* **459**, 214380 (2022).
19. Zhou, Y. *et al.* A solution-processable natural crystal with giant optical

anisotropy for efficient manipulation of light polarization. *Nat. Photon.* **18**, 922–927 (2024).

20. Gao, J., Wang, C., Sow, C. H., Zhang, Q. & Poh, E. T. Ultrathin Quarter-Waveplates Based on Two-Dimensional Anisotropic $NbOCl_2$. *Nat Commun* https://doi.org/10.1038/s41467-026-70788-3 (2026) doi:10.1038/s41467-026-70788-3.

21. Zhao, Y., Belkin, M. A. & Alù, A. Twisted optical metamaterials for planarized ultrathin broadband circular polarizers. *Nat Commun* **3**, 870 (2012).

22. Askarpour, A., Zhao, Y. & Alù, A. Wave propagation in twisted metamaterials. *Physical Review B* **90**, (2014).

23. Han, Z., Wang, F., Sun, J., Wang, X. & Tang, Z. Recent Advances in Ultrathin Chiral Metasurfaces by Twisted Stacking. *Advanced Materials* **35**, 2206141 (2023).

24. Yu, N. & Capasso, F. Flat optics with designer metasurfaces. *Nature Mater* **13**, 139–150 (2014).

25. Cui, T. J., Liu, S. & Zhang, L. Information metamaterials and metasurfaces. *J. Mater. Chem. C* **5**, 3644–3668 (2017).

26. Luo, X., Tsai, D., Gu, M. & Hong, M. Subwavelength interference of light on structured surfaces. *Adv. Opt. Photon.* **10**, 757 (2018).

27. Geim, A. K. & Grigorieva, I. V. Van der Waals heterostructures. *Nature* **499**, 419–425 (2013).

28. Ermolaev, G. A. *et al.* Giant optical anisotropy in transition metal dichalcogenides for next-generation photonics. *Nat Commun* **12**, 854 (2021).

29. Yang, L. *et al.* Weak-disturbance imaging and characterization of ultra-confined optical near fields. *Light Sci Appl* **14**, 358 (2025).

30. Niu, S. *et al.* Giant optical anisotropy in a quasi-one-dimensional crystal. *Nat. Photon.* **12**, 392–396 (2018).

31. Li, L. *et al.* Emerging in-plane anisotropic two-dimensional materials. *InfoMat* **1**, 54–73 (2019).

32. Tang, J. *et al.* Optical anisotropy of Bi_2SeO_5 and near-field characterization of its waveguide modes. *Nanoscale* **17**, 18220–18228 (2025).

33. Guo, Q. *et al.* Colossal in-plane optical anisotropy in a two-dimensional van der Waals crystal. *Nat. Photon.* **18**, 1170–1175 (2024).

34. Guo, Q. *et al.* Colossal in-plane optical anisotropy in a two-dimensional van der Waals crystal. *Nat. Photon.* **18**, 1170–1175 (2024).

35. Guo, Q. *et al.* Ultrathin quantum light source with van der Waals $NbOCl_2$ crystal. *Nature* **613**, 53–59 (2023).

36. Wang, Y., Wu, Y. & Sun, M. Indirect and direct electronic transitions and electron transport properties of van der Waals $NbOCl_2$. *Phys. Chem. Chem. Phys.* **26**, 22518–22528 (2024).

37. Ye, L. *et al.* Manipulation of nonlinear optical responses in layered ferroelectric niobium oxide dihalides. *Nat Commun* **14**, 5911 (2023).

38. Li, Y. *et al.* Hyperbolic localized plasmons and twist-induced chirality in an anisotropic 2D material. *Nat Commun* **17**, 2716 (2026).

39. Gao, H., Ding, C., Sun, L., Ma, X. & Zhao, M. Robust broadband directional plasmons in a $MoOCl_2$ monolayer. *Phys. Rev. B* **104**, 205424 (2021).

40. Venturi, G., Mancini, A., Melchioni, N., Chiodini, S. & Ambrosio, A. Visible-frequency hyperbolic plasmon polaritons in a natural van der Waals crystal. *Nat Commun* **15**, 9727 (2024).

41. Ruta, F. L. *et al.* Good plasmons in a bad metal. *Science* **387**, 786–791 (2025).

42. Li, Y. *et al.* Broadband near-infrared hyperbolic polaritons in $MoOCl_2$. *Nat Commun* **16**, 6172 (2025).

43. Zhang, Y. *et al.* Manipulating Hyperbolic Plasmon Polaritons at Near-Infrared in an Anisotropic van der Waals Crystal. *Nano Lett.* **25**, 15534–15541 (2025).

44. Zheng, Z. *et al.* A mid-infrared biaxial hyperbolic van der Waals crystal. *Science Advances* https://doi.org/10.1126/sciadv.aav8690 (2019) doi:10.1126/sciadv.aav8690.

45. Zhao, J. *et al.* Highly anisotropic two-dimensional metal in monolayer $MoOCl_2$. *Phys. Rev. B* **102**, 245419 (2020).

Author contributions

Q.G., and G.L. hosted the project. Y.L. and G. Z. conceived the idea. S.H., G.Z. and X.M. conducted the numerical simulations. S.H., M.D. and Y.X. conducted the samples. S.H., G.Z., X.M., Y.X., and Z.C. conducted the sample characterizations and measurements. S.H., G.Z. and X.M. conducted the data processing and analysis. All authors contributed to writing the original draft, reviewing, and editing the manuscript.

Competing interests

The authors declare no competing interests.

Supplementary Files

This is a list of supplementary files associated with this preprint. Click to download.

- supportinformationUltrathinHighPerformanceCircularWavePlateBasedonNaturalvanderWaalsCrystals.pdf